ACS NANO

www.acsnano.org

Shaping the Emission Directivity of Single Quantum Dots in Dielectric Nanodisks Exploiting Mie Resonances

Cristina Cruciano, Davide Rocco, Armando Genco,* Andrea Tognazzi, Andrea Locatelli, Luca Carletti, Alexey Fedorov, Chiara Trovatello, Giuseppe Di Blasio, Ilaria Bargigia, Charalambos Louca, Paolo Gubian, Giulio Tavani, Luca Lovisolo, Artur Tuktamyshev, Lucio C. Andreani, Matteo Galli, Giulio Cerullo, Giuseppe Leo, Stefano Sanguinetti, Costantino De Angelis, and Monica Bollani

Cite This: *ACS Nano* 2025, 19, 3500−3509

Read Online

ACCESS | Metrics & More | Article Recommendations | Supporting Information

ABSTRACT: **Manipulating the optical landscape of single quantum dots (QDs) is essential to increase the emitted photon output, enhancing their performance as chemical sensors and single-photon sources. Micro-optical structures are typically used for this task, with the drawback of a large size compared to the embedded single emitters. Nanophotonic architectures hold the promise to modify dramatically the emission properties of QDs, boosting light−matter interactions at the nanoscale, in ultracompact devices. Here, we investigate the interplay between gallium arsenide (GaAs) single QDs and aluminum gallium arsenide (AlGaAs) nanostructures, capitalizing on the Kerker condition for precise control of the QD emission directivity. An extensive analysis of the photoluminescence spectra of several QDs embedded in nanodisks revealed a pronounced directivity enhancement due to the Kerker effect, confirmed by theoretical simulations, resulting in a 14-fold increase of emitted intensity. Angle-resolved spectroscopy experiments also proved that the integration of GaAs QDs within nanostructures determines a precise angled emission, offering a distinctive avenue for manipulating the spatial characteristics of emitted light by exploiting Mie resonances. This work contributes to the optimization of QD integration in nanostructures and suggests potential improvements for applications in optical communications.**

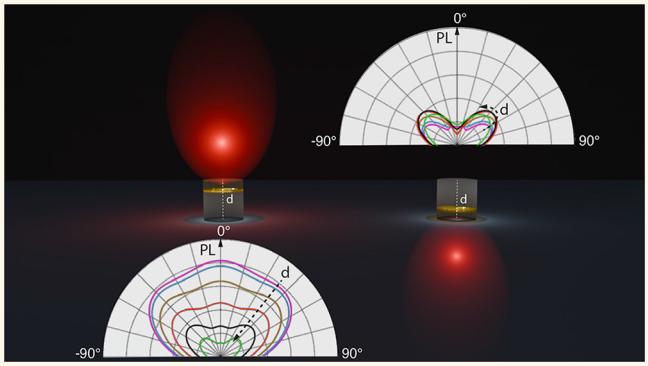

KEYWORDS: *Mie resonances, quantum dots, Kerker condition, microphotoluminescence, Fourier imaging*

INTRODUCTION

The convergence of quantum optics and nanophotonics has sparked countless innovations and discoveries, propelling the field toward unprecedented precision in the control of light−matter interactions at the nanoscale. Quantum dots (QDs), as versatile single-photon emitters, have become a fundamental building block for photonic quantum information, communication, and sensing technologies.[1] However, to fully exploit their quantum nature, researchers are increasingly focused on overcoming inherent challenges, such as the effective control and manipulation of QD emission.[2,3] To this aim, it is of key importance to engineer the photonic landscape around the QD on a nano- or microscale, channeling the emitted photons into highly directional optical modes and out-coupling them for external use in quantum computation and communication.[4] Several micro-optical architectures have been proposed to maximize the overall photon extraction efficiency, keeping a high degree of single-photon indistinguishability (up to 99%).[5] Gate-tunable open microcavities,[6] micropillars,[7−9] and photonic crystal waveguides[10−13] are among the best structures used for optimized QD-based single-photon sources, reaching end-to-end photon generation efficiencies exceeding 50%.[6] Photonic nanostructures further expand the possibilities to shape the light−emitter interactions acting on the local

Received: September 21, 2024
Revised: December 23, 2024
Accepted: December 27, 2024
Published: January 11, 2025

https://doi.org/10.1021/acsnano.4c13327
ACS Nano 2025, 19, 3500−3509

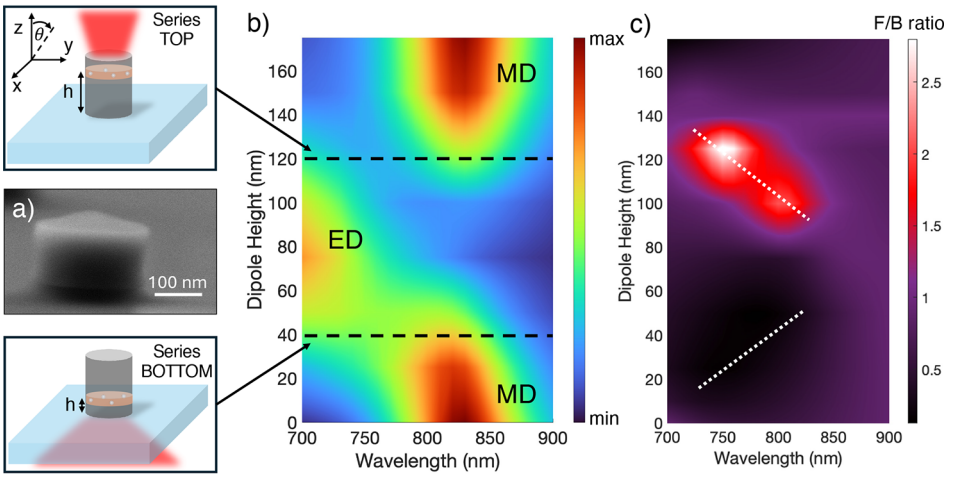

Figure 1. (a) Scanning electron microscopy (SEM) image of fabricated nanodisks after all fabrication processes. Due to the low density and nanometric size of QDs, it is not possible to visualize their presence in a high-resolution SEM image. (b) Calculated normalized scattering cross section as a function of the wavelength and dipole height. The black dashed lines indicate the two considered QD positions, as schematically illustrated by the two insets with the sketch of the QD-loaded nanodisks of series TOP and BOTTOM. (c) Calculated ratio between the far field radiated toward air and the substrate (F/B ratio) as a function of the wavelength and dipole height. The white dotted lines highlight the high directivity regions.

electromagnetic environment of the QD at the nanoscale, with the additional advantage of shrinking the size of the device to the submicrometer scale, useful for on-chip integration.

In this context, the Kerker condition has risen to prominence as a valid tool for manipulating the electromagnetic landscape within nanostructures[14,15] and at microwave frequencies.[16] Originally conceived for the control of classical light scattering, the Kerker condition has been recently predicted to be extremely useful in the quantum domain also.[17] This innovative paradigm introduces a promising route toward controlling emission directions from QDs by strategically integrating them with optical nanostructures. The Kerker effect, characterized by a significant asymmetry in forward-to-backward electromagnetic scattering, is a fundamental and versatile physical mechanism for directing the scattering of an electromagnetic plane wave using Mie resonant particles. This unidirectional scattering mechanism is based on the interference of electromagnetic multipolar moments induced in the Mie scatterers.[15] Thus, by optimizing the excited multipoles in the nanostructure, it is possible to obtain zero-back scattering or zero-forward scattering conditions. While the Kerker condition has been extended to higher-order multipoles, the case of the most immediate practical realization is the one that involves the electric dipole (ED) and magnetic dipole (MD) resonances.[18−20] When these two multipoles have the same amplitude and zero phase difference, we can obtain a Kerker-type emission in the forward direction (first Kerker condition), whereas if the phase difference is π, the radiation is in the backward direction (second Kerker condition).[21] A moderately high forward-to-backward scattering ratio can be achieved under the first Kerker condition. Let us underline that the first experimental demonstration of zero backscattering due to Kerker conditions in nanoantennas was reported in ref 18 for a regular arrays of GaAs pillar structures obtained by reactive ion etching synthesis procedure.

All-dielectric nanostructures showed a wide range of applications concerning the optimization of their radiation emission both in isolated and metasurface configurations.[22−28] By manipulating the scattering properties of dielectric nanoparticles, researchers theoretically proposed to sculpt the emission characteristics of QDs with unprecedented precision.[21] However, there are only few experimental results showing the interaction of quantum sources with dielectric nanoantennas.[29−33] For instance, in ref 34, the authors report a soft-stamping method to selectively print a layer of QDs on top of an array of silicon nanodisks to accurately control the QD emission shape through engineered coupling of the QDs to the Mie resonances supported by the dielectric nanocylinders, demonstrating a 10-fold increase in the upward direction.

Here, we test both theoretically and experimentally the behavior of a few GaAs-based QDs working as quantum emitters embedded within AlGaAs dielectric nanoresonators and exploit the Kerker condition to modify the emission directivity based on the position of the QDs within the nanodisks. By employing a novel fabrication method, we create AlGaAs nanodisks on a AlO_x transparent layer with a low number of QDs (about 8−12 dots for the cylinder) located at two different heights within the pillar, which correspond to forward and backward scattering Kerker conditions. Angle-resolved photoluminescence (PL) spectroscopy reveals a strong dependence of the angular emission pattern on the position of the QDs within the base area of the pillar. Performing a statistical analysis on more than 150 QDs, we observe a dramatic enhancement of the PL intensity by more than 1 order of magnitude when the emitters reside close to the top of the nanodisks, demonstrating the efficacy of the Kerker effect. The integration of QDs with nanostructures leveraging the Kerker condition not only advances our fundamental understanding of light−matter interactions but also opens pathways to practical applications, from quantum information processing to advanced sensing technologies.

RESULTS AND DISCUSSION

Numerical Simulation. In order to emulate the scattering behavior of the proposed active photonic system, we performed finite-element simulations in Comsol Multiphysics. In the numerical study, we consider an AlGaAs cylinder with a radius of 110 nm and a height of 175 nm on a low refractive

https://doi.org/10.1021/acsnano.4c13327
ACS Nano 2025, 19, 3500−3509

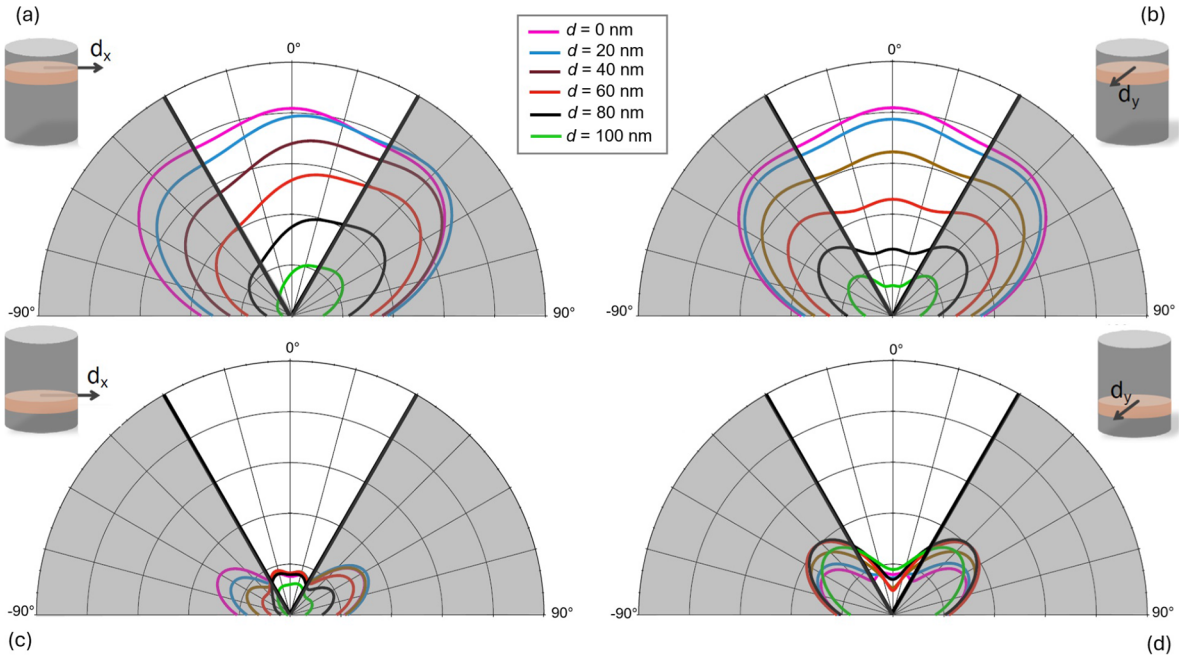

Figure 2. Calculated radiation pattern in the air region as a function of the QD displacement along the *x* (left panels) or *y* axis (right panels) for the two reference heights of series TOP (a, b) and BOTTOM (c, d) highlighted by the insets. The gray area indicates the region outside the NA used in the experiment.

index (n = 1.6) substrate. For the dispersion of AlGaAs, we consider the permittivity values as in ref 35. The QD source is modeled as a point-like x-polarized electric dipole positioned at the center of the cylinder at different heights (see insets of Figure 1a). From our simulations, we choose two different vertical positions for the QDs to better satisfy the Kerker condition in the fabricated nanodisks, named series TOP and series BOTTOM. In order to find such values, we performed a parametric study as a function of both the QD vertical position and the emission wavelength. The obtained wavelength and position-dependent scattering cross section are shown in Figure 1b. The graph highlights three zones of maximum emission that correspond to the excitation of the ED and MD resonance modes in the AlGaAs cylinder. The dashed black lines indicate the QD positions at which the amplitudes of ED and MD are the same at a wavelength of 760 nm, corresponding to the fabricated series TOP and BOTTOM. It should be noted that the excitation of these resonances is not perfectly symmetrical with respect to the variation in the height position of the QD due to the presence of the substrate underneath the cylinder. The ideal Kerker condition is achieved when the ED and MD have the same amplitude and zero or π rad phase difference to reach the unidirectional emission toward the air or substrate region, respectively. As reported in ref 21, the performance in terms of emission directivity can be expressed by a front-to-back (F/B) ratio, defined as the ratio between the magnitude of the electric far field at $\theta = 0$ rad and at $\theta = \pi$ rad, where θ is defined as in the reference system of Figure 1. In particular, Figure 1c shows that when the QD is positioned at a height of about 120 nm (series TOP) from the base of the cylinder, the F/B ratio is maximum, while it is minimum when the position of the QD is 40 nm (series BOTTOM) around the wavelength of 760 nm. These preliminary simulations confirm how it is possible, depending on the QD vertical position, to engineer the emission from the nanostructure by almost fulfilling the first Kerker condition. In particular, for positions of the QD around 120 nm in height, the light radiation is redirected mainly toward the air region (i.e., ED ≈ MD), while for heights of around 40 nm, the emission is mainly directed toward the substrate (i.e., ED ≈ −MD). Furthermore, in the simulations, we also considered the more realistic case of a finite thickness (equal to 1 μm) for the AlO_x substrate with an underlying GaAs layer. For the latter case, the emission properties do not undergo notable variations with respect to the case of a single AlO_x layer; therefore, we considered in the subsequent numerical analysis the less time-consuming computational case of the semi-infinite AlO_x substrate only. We also numerically evaluate the Purcell factor (PF) from our platform under Kerker conditions. The PF reaches a value close to 3.5 for the bottom height QD around an incident wavelength of 760 nm. Let us point out that for the proposed design, we are working in the Kerker regime, where both the ED and MD resonances are equally excited but not at their maximum. For instance, the PF values at the exact ED and MD reach 4.7 and 6.4, respectively. Therefore, our platform has a PF that is lower than the one reported in state-of-the-art papers.[36,37] This is mainly due to the modest field enhancement factors achievable in our fully dielectric structures when working around low quality factor (QF) resonances, such as ED and MD. To boost the electromagnetic concentration, one may consider the interaction with higher QF resonances; however, this may complicate the design, especially the fulfillment of the Kerker condition. Therefore, we limit ourselves to the dipolar mode interaction. However, differently from ref 36, the proposed structure is not affected by ohmic losses since no metallic elements are used. Thus, it is potentially suited to attain a system quantum efficiency, defined as the ratio of radiative power to total dissipated power, equal to the one of the isolated emitters.

In addition, we analyze how the position of the QD within the base area of the nanodisk influences the radiation in terms

https://doi.org/10.1021/acsnano.4c13327
ACS Nano 2025, 19, 3500−3509

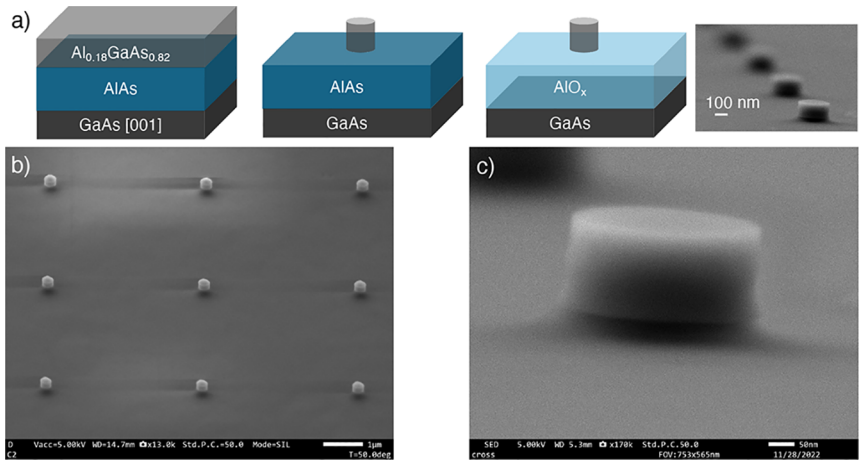

Figure 3. (a) Representation of the fabrication steps starting from the MBE growth, EBL and RIE processes, and finally selective oxidation treatment. (b) SEM tilted view image of patterned cylinders, whose radius changes every line thanks to the optimized lithographic tuning. (c) High-resolution SEM image of a single AlGaAs cylinder, inside which are placed a few GaAs QDs, positioned above the oxidized AlO_x layer.

of scattered power and emission directivity. For the two reference heights (120 and 40 nm for series TOP and BOTTOM, respectively), we evaluated the emission variation of the scattered light from our platform as a function of the offset of the QD, along the x or y axis, with respect to the axis of the nanoresonator (additional results for randomly distributed QDs are reported in the Supporting Information). The results of this study are depicted in the polar plots of Figure 2, where the gray shaded areas represent the angular range outside the numerical aperture (NA) of the objective used in the experiments, equal to 0.5. In particular, for the TOP series, when the QD is moved along the x axis from the center (Figure 2a), a slightly angled radiation pattern is observed, with a maximum emission that goes from the vertical direction ($\theta = 0$ rad) up to approximately $\theta = \pi/4$ rad when the QD is close to the border of the cylinder. Instead, moving the QD along the y direction degrades the unidirectional emission, and for $d \geq 70$ nm, the emission side lobes become predominant (Figure 2b). This behavior is due to the excitation of higher-order modes in the cylinder. For the QD in series BOTTOM, minor lobes are emitted into the air region since the main emission is radiated toward the substrate (Figure 2c,d).[21]

Fabrication. The investigated nanostructures are fabricated by a combination of molecular beam epitaxy (MBE), electron beam lithography (EBL), inductively coupled plasma reactive ion etching (ICP-RIE), and local oxidation thermal processes. A schematic of the sample structures is shown in Figure 3a.

The samples are grown in a conventional MBE system on GaAs(001). The growths are performed using a valved cell for the optimal control of the As_4 flow and monitored by in situ reflection high-energy electron diffraction (RHEED). After the oxide desorption in an As atmosphere at 580 °C, an atomically smooth surface is prepared by growing a ∼250 nm thick GaAs buffer layer with a rate of 0.5 monolayer (ML)/s. Then, a 1 μm thick AlAs film is deposited at $T = 620$ °C with a rate of 0.5 ML/s. This structure stack is identical for the two growth series (indicated as TOP and BOTTOM) and, following a selective external oxidation process, is used for optical insulation. At the same temperature, an AlGaAs layer with an 18% Al content of 40 nm (series BOTTOM) or 115 nm (series TOP) is deposited. On top of the AlGaAs structure, a layer of self-assembled QDs is deposited using the droplet epitaxy (DE) technique,[38] which permits the fabrication of strain-free[39] and strained[40] III−V QDs with high control of size[41] and symmetry.[42] The DE is a two-step growth process, which consists of (1) the formation of tiny droplets of group III metal by irradiation of the metal on the substrate surface in the absence of As and (2) annealing of the droplets in an As atmosphere to convert them in three-dimensional nanoislands.[43] For the DE step, the substrate temperature is decreased to 170 °C, and the As valve is closed at 420 °C in order to deplete the growth chamber of the As molecules. The RHEED pattern shows a c(4 × 4) surface reconstruction. Ga adatoms are deposited on the AlGaAs surface at a temperature of 170 °C with a flow of 0.1 ML/s. By this condition, we expect to have a QD density of about 400 droplets per square micron. The first monolayer of Ga, interacting with the As-rich c(4 × 4) reconstructed surface, establishes a Ga-stabilized (3 × 6) reconstruction.[44] The droplets are subsequently formed by the remaining Ga atoms. In total, 2.5 MLs of Ga were deposited and self-assembled in droplets. Then, the Ga droplets are exposed to an As beam equivalent pressure of 5×10^{-5} Torr at 170 °C for 3 min to crystallize them into GaAs nanoislands.[43] Subsequently, the nanocrystals undergo a flash procedure consisting of 10 min at 380 °C in an As pressure of 4×10^{-6} Torr. The GaAs dots are then covered by 30 MLs of AlGaAs (∼8 nm) by migration-enhanced epitaxy.[45] Finally, the temperature is increased up to 620 °C, and AlGaAs alloys with 18% Al are deposited on top of the QD layer to reach a total thickness of 175 nm. Both structures (TOP and BOTTOM series) are capped with ∼5 nm of GaAs to prevent the oxidation process. The EBL is carried out in order to define circular structures with radii varying from 80 to 140 nm. A double layer of poly(methyl methacrylate) (PMMA) diluted in chlorobenzene, respectively, at 3.5 and 1.5% is employed. The dose used at 30 kV for the structures is 350 $\mu C/cm^2$ for larger diameters, increased to 390 μ/cm^2 for smaller ones. After exposure, PMMA is developed for 90 s in a diluted solution of methyl isobutyl ketone and isopropanol in a 1:3 ratio to obtain well-defined profiles.[46] The pattern is transferred down to the bottom AlAs by nonselective ICP-RIE with $SiCl_4$:Ar chemical treatment. The etching depth of 175 nm for both series is controlled by laser interferometry, defining the AlGaAs

https://doi.org/10.1021/acsnano.4c13327
ACS Nano 2025, 19, 3500−3509

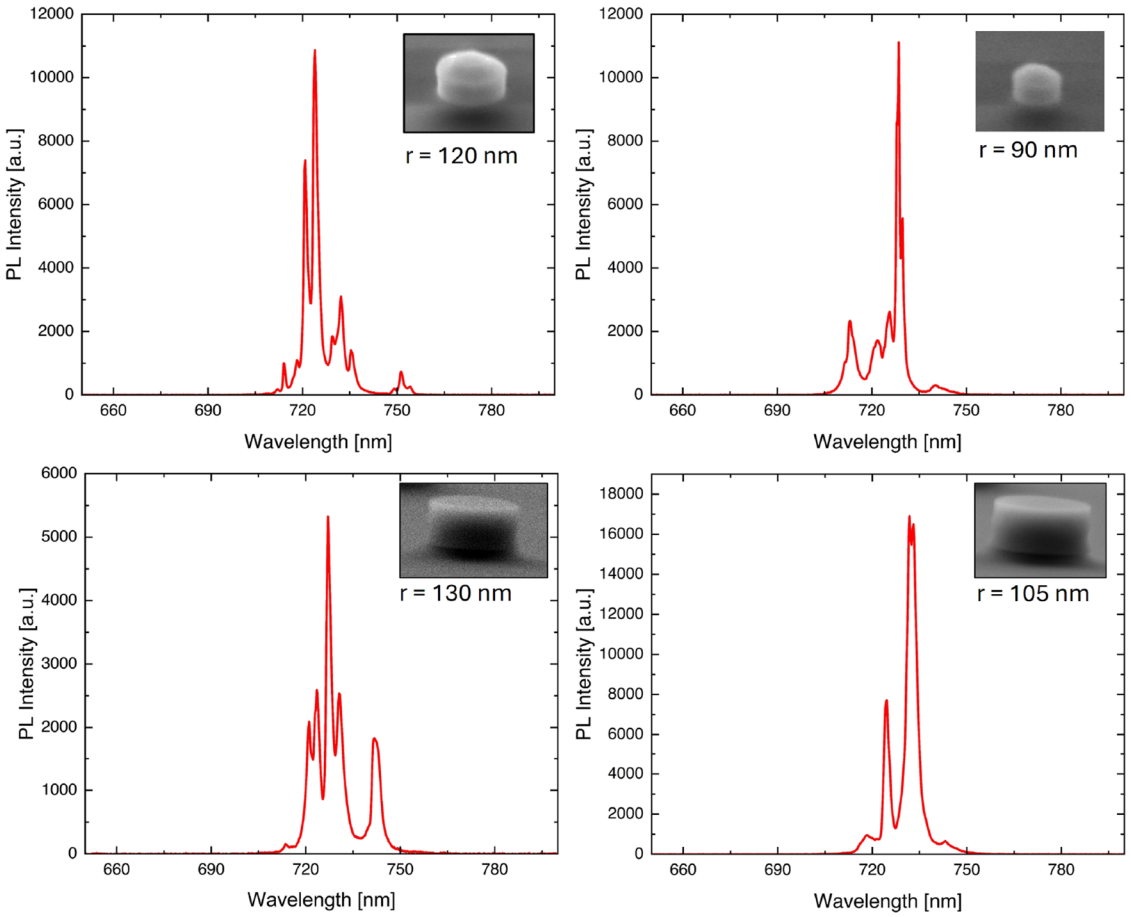

Figure 4. PL spectra collected from single nanodisks for different patterned areas in the TOP series. Nanodisks with different radii are analyzed, showing PL signals of different intensities and peak positions, mainly due to the slightly different dimension of QDs present in the cylinder and their position with respect of the cylinder axis.

nanocylinders. The AlAs layer is then thermally oxidized into AlO_x, resulting in an optical confinement in the active layer because of the refractive index difference between $Al_{0.18}Ga_{0.82}As$ ($n \approx 3.3$) and AlO_x ($n \approx 1.6$).[47] The selective oxidation of the Al-rich layers is performed in water vapor at a temperature of 300 °C, which leads to the formation of aluminum oxide.[48] Using nanolithographic tuning, cylinders with radii just a few nanometers apart are realized, covering surfaces of over 100 square micrometers and periods of 3 μm (Figure 3b). The optimization of the dry etching process is visible in the high-resolution SEM image of a single cylinder, where lateral etching imperfections are negligible (Figure 3c). More details on the materials used in the fabrication process can be found in the Materials and Methods section.

Spectroscopy Experiments. To investigate the directivity and the angular emission pattern of the QDs embedded in the nanodisks, we performed PL spectroscopy both in real space and in Fourier space (k-space) at 8 K using a custom-made microscopy setup, equipped with a 50× objective lens (NA: 0.5) and a 630 nm CW laser for excitation (see more details in the Materials and Methods section and Supporting Information). Low-temperature PL is necessary to achieve efficient emission from GaAs/AlGaAs QDs since the exciton binding energy is <10 meV.[49] In fact, we could not detect any appreciable PL signal from the QDs at room temperature. Four PL spectra measured in real space, exemplary for the QD emission in a series of cylinders with different radii, are reported in Figure 4. Each PL spectrum shows a few peaks due to the emission of single QDs. The single-photon emission properties of our QDs were tested by performing second-order correlation g^2 measurements on narrow PL lines, which showed moderate antibunching (see the Supporting Information for more details). The different emission energies depend on the slightly different sizes of the QDs and their positions relative to the center of the cylinder. The QDs embedded closer to the walls have lower PL intensity compared to QDs positioned in the center due to nonradiative recombination processes. We use k-space spectroscopy since it allows us to easily characterize both the spectrum and the angular pattern of the light emitted/transmitted/reflected from optical micro- and nanostructures and metasurfaces in an angular range within the NA of the objective.[50] In our setup, the PL emitted from the sample is collected by the excitation objective and sent to a spectrometer equipped with a CCD camera. By adding a Fourier lens in the detection path of the microscope, we image the back focal plane of the objective lens, defined as the plane normal to the optical axis of the lens situated at a focal distance behind the objective. On this plane, every point corresponds to a specific value of the incoming light wavevector k, proportional to the angle of light rays measured from the lens axis. Given the NA of our objective, the detected angular field of view (FOV) spans from 0 to 30°. By closing the slit of the spectrometer, we select just a vertical slice of the Fourier-plane image, which is then diffracted by grating of the

https://doi.org/10.1021/acsnano.4c13327
ACS Nano 2025, 19, 3500−3509

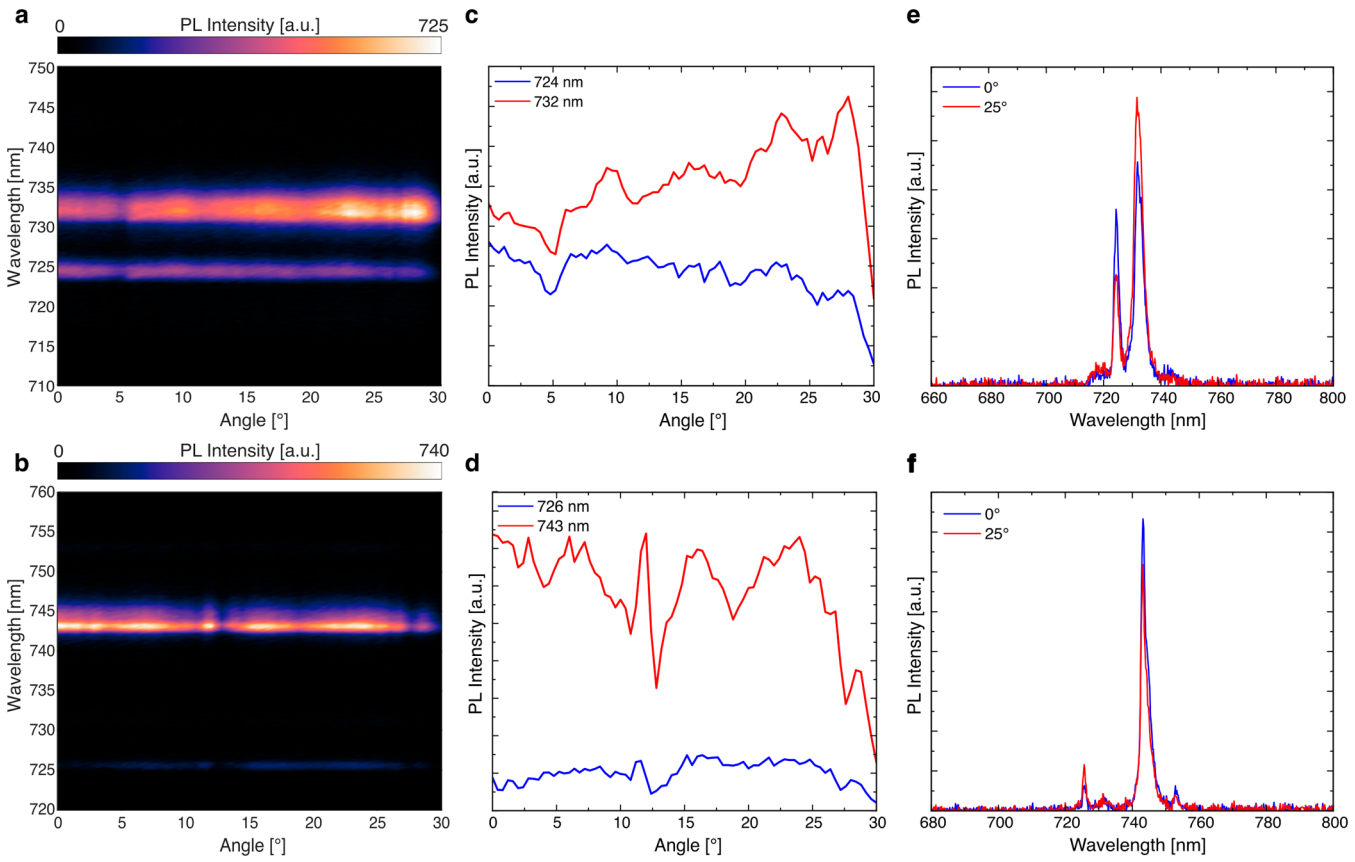

Figure 5. (a, b) PL *k*-space maps showing the emission lines of nanodisks with QDs in series TOP (a) and BOTTOM (b). (c, d) Horizontal cross sections of panels (a) and (b) taken at PL peak wavelengths of the QDs showing the angular emission pattern. (e, f) Vertical cross sections of panels (a) and (b) showing the PL spectra at different angles, at 0° (e) and 25° (f).

spectrometer (Figure S1). This results in a map of PL intensity as a function of θ_y and wavelength, recorded by the camera.

Figure 5a,b shows the PL maps as a function of angle and wavelength recorded for two nanodisks, one for the TOP series (a) and one for the BOTTOM series (b). It can be noticed that the intensity of the QD emission varies as a function of the angle. This trend is better represented in Figure 5c,d, which shows horizontal cross sections of the maps in Figure 5a,b taken at the peak wavelength of the main emission lines. The abrupt changes in intensity visible in the curves are attributed to small defects in the optical elements used in the setup. It can be seen that, even inside the same nanodisk, the emission follows different angular patterns for different QDs, increasing or decreasing in intensity with the angle. Figure 5e,f shows vertical cross sections of the maps in Figure 5a,b taken at 0 and 25°, where the difference in intensity between the QD emission lines can be appreciated more clearly. On the other hand, the QD spectral shape shows negligible variations by changing the angle. Comparing these results with the simulations in Figure 2, we argue that an increase of emission at higher angles can be related to QDs positioned closer to the edge of the nanodisks, e.g., the QD emitting at 732 nm in Figure 5a,c,e. Therefore, angle-resolved PL emission spectroscopy can help to discern the position of single QDs within the base area of each nanodisk, which cannot be controlled at the fabrication level and is very difficult to characterize without using more complex and often invasive techniques.

We performed a statistical analysis of the collected PL spectra in real and Fourier space on several nanocylinders with different radii and with QDs positioned at the top and at the bottom. Figure 6a shows the distribution of the PL peak intensities as a function of the peak wavelength for more than 150 QD emission lines extracted from the PL real-space measurements on nanodisks of series TOP and series BOTTOM (red and blue dots in Figure 6a, respectively) with different radii. Although the intensity distribution is quite broad for both the series, the QDs in series TOP are clearly brighter than the ones in series BOTTOM. In fact, the calculated average intensity of all the QDs in the former series is about 1 order of magnitude higher ($\frac{< I_{top} >}{< I_{bottom} >} = 7.1$) than in the latter (dashed lines in Figure 6a). By moving away from the Kerker condition, around 725 nm, for example, this statement still holds in part; in fact, while the series TOP QDs are still brighter than the bottom one, the ratio between the average PL intensity is lower than the ratio calculated considering the whole emission spectral range ($\frac{< I_{top} >}{< I_{bottom} >} = 4.8$).

We compare these results with the simulated scattered power for the TOP and BOTTOM series, as a function of the distance of the QD from the central axis of the pillar (Figure 6b). Interestingly, even by moving the QD from the center of the nanodisk up to 40 nm (both along the *x* or *y* direction), the scattered power of series TOP is always more than an order of magnitude higher compared to series BOTTOM, as a consequence of the Kerker effect. This represents an indication that the QDs positioned around the center of the nanodisk, when placed at the designated heights, may have a good

https://doi.org/10.1021/acsnano.4c13327
ACS Nano 2025, 19, 3500−3509

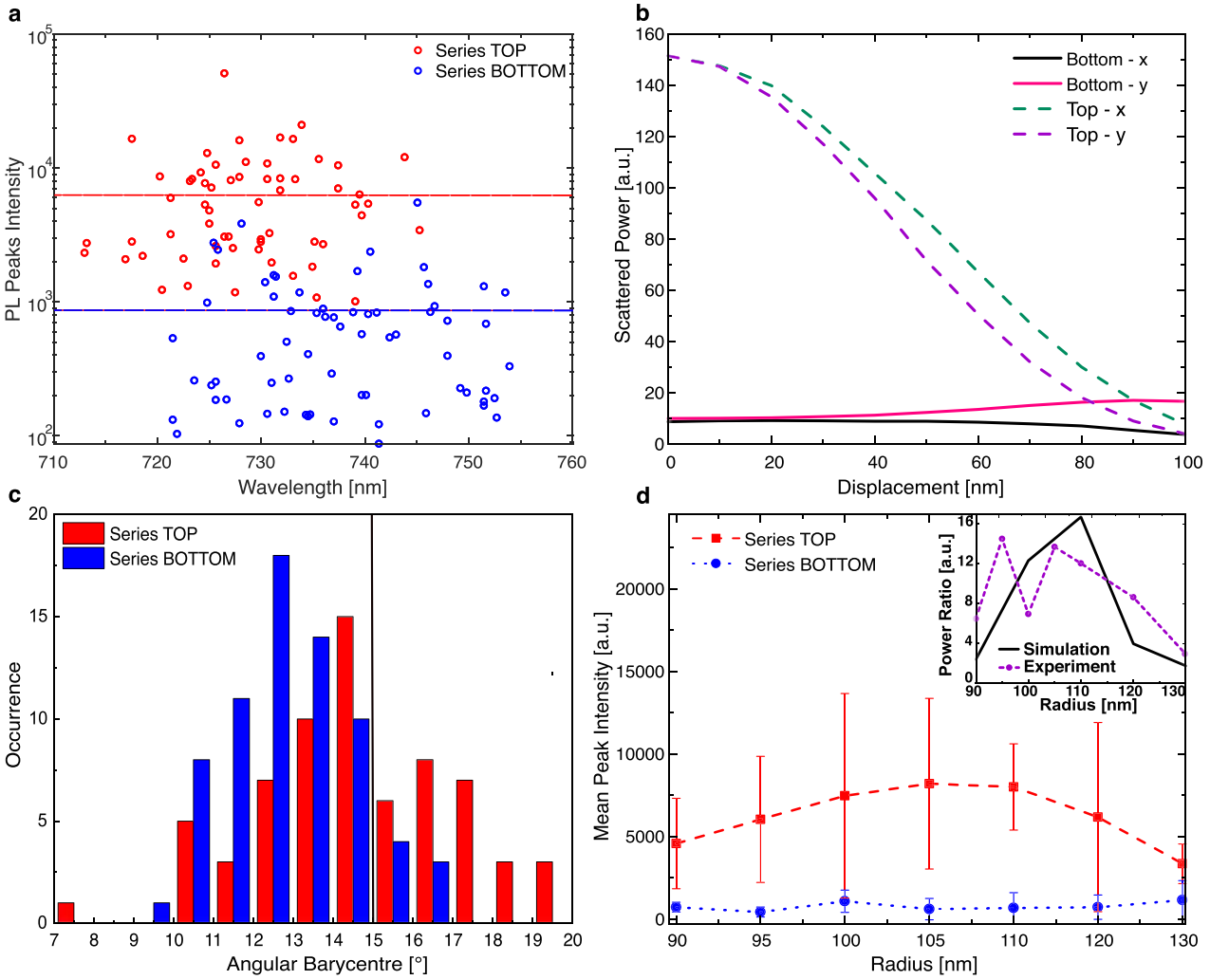

Figure 6. (a) QD PL peak intensity as a function of the peak wavelength extracted from the real-space PL measurements for both the series (red dots: series TOP; blue dots: series BOTTOM). The dashed lines refer to the averaged PL intensity for the two series. (b) Simulations of the scattered power of the QDs as a function of the displacement from the center of the nanodisk for the series with QDs on top (dashed lines) and at the bottom (solid lines). (c) Histograms of the angular barycenter calculated for every QD emission pattern taken from the *k*-space measurements. The black vertical line is at half of the angular FOV. For series TOP (red columns), the distribution peaks between 14 and 15°, while for series BOTTOM (blue columns), the distribution is shifted between 12 and 13°. (d) Average PL peak intensity of QDs as a function of the nanodisk radius for the TOP and BOTTOM series (red and blue squares). The error bars are the standard deviations extracted from the statistics. Inset: Simulated and experimental PR versus the nanodisk radius.

coupling with the ED and MD resonances and consequently a Kerker-like emission.

For every measured QD angular emission pattern, taken from the horizontal cross section of the PL Fourier maps at the QD peak wavelengths, e.g., Figure 5c,d, we calculated the weighted averaged angle (or angular barycentre), defined as the product between the PL intensity at each angle and the emission angle, divided by the total PL intensity emitted over the spanned angular range. In the sample with the QDs on top (red histogram in Figure 6c), the distribution shows a maximum between 14 and 15° at roughly half of the total angular FOV (30°). On the other hand, for the sample with the QDs at the bottom (blue histogram in Figure 6c), the distribution peak is shifted closer to the normal direction between 12 and 13°, suggesting a QD emission directionality more pronounced toward small angles in the latter configuration. This behavior is due to the nonsymmetric QD distribution inside the nanocylinder. The QDs are placed randomly across the base area of the nanodisks and, according to our simulations in Figure 2, the maximum of the emission inside the NA is found to be close to zero angle in series BOTTOM even for large displacements along the *x* axis. Therefore, for off-centered QDs, the emission is expected to be distributed over smaller angles for series BOTTOM compared to series TOP (see, for instance, the green and black curves of Figure 2), still resulting in a much higher overall scattered power in the latter sample.

Figure 6d plots the average PL intensity of the two series as a function of the nanodisk radius. Regardless of the radius dimension, the PL peak intensity in the TOP series is always much higher than when the QDs are located at the bottom. The maximum power ratio (PR), defined as the average PL intensity of series TOP divided by the one of the BOTTOM series, is about 14 for radii between 95 and 105 nm, where the Kerker condition is most effective.

To further validate the measurements, we numerically computed the PR as the scattered power for the QD at the top position in a NA equal to 0.5 divided by the scattered

https://doi.org/10.1021/acsnano.4c13327
ACS Nano 2025, 19, 3500−3509

power for the QD at the bottom position in the same NA as a function of the AlGaAs pillar radius (see the inset of Figure 6d). The maximum theoretical PR is reached for a radius of 110 nm, with a value very close to the experimental one. We underline that this small geometrical mismatch with respect to the nominal value of the AlGaAs pillar radius is completely within the fabrication tolerance inaccuracy for such structures.

CONCLUSIONS

In this work, we have shown how the integration of GaAs QDs in AlGaAs nanostructures can be used for manipulating the emitted light by exploiting the Mie resonances sustained inside the AlGaAs volume for a strong enhancement of the outcoupled PL. After presenting the theoretical background, we fabricated the optimized structures based on numerical simulations and measured their emission properties. Changing the vertical position of the dots by just 80 nm, we found a dramatic increase in the PL directivity from QDs in forward versus backward scattering Kerker conditions. Moreover, we have shown how small variations in the QD position within the nanodisk can substantially modify the angular emission pattern. The experimental results align very well with the theoretical computations. Our results may open new routes for light emission control in single emitters with possible applications in integrated optics, communication, and sensing. The interaction between QDs and optical nanostructures, guided by the principles of the Kerker condition, has the potential to boost QD emission in the dynamic interplay between light and matter on the nanoscale.

MATERIALS AND METHODS

For nanofabrication, we used a GaAs epi-ready undoped single wafer, (110) ± 0.1°, with a resistivity of 10^7 Ω − cm, purchased from AXT company. For the double PMMA layer used in the EBL step, we used ARP 642.04 (200 K) for the first layer and ARP 672.02 (950 K) for the second film. After exposure, a thin SiO_2 film (about 30 nm) was deposited on the exposed circular areas and used as a mask during the subsequent etching process.

To perform PL measurements, we employed a custom-made microscopy setup. We excited the samples using a 630 nm CW laser, delivered to a 50× objective lens (NA: 0.5). The sample was placed in a closed loop He cryostat reaching 8 K. The sample's emission was collected in back reflection. We used a standard tube lens for real-space measurements or an additional Fourier lens for Fourier-space measurements. The PL spectra and images were recorded using a spectrometer and a CCD camera. More details can be found in the Supporting Information.

ASSOCIATED CONTENT

Supporting Information

The Supporting Information is available free of charge at https://pubs.acs.org/doi/10.1021/acsnano.4c13327.

Scheme of the experimental setup; simulations of randomly distributed QDs; antibunching and PL lifetime experiments; and additional PL angular patterns from QDs (PDF)

AUTHOR INFORMATION

Corresponding Author

Armando Genco − *Department of Physics, Politecnico of Milano, 20133 Milano, Italy;* orcid.org/0000-0002-1292-2614; Email: armando.genco@polimi.it

Authors

Cristina Cruciano − *Department of Physics, Politecnico of Milano, 20133 Milano, Italy*

Davide Rocco − *Department of Information Engineering, University of Brescia, 25123 Brescia, Italy*

Andrea Tognazzi − *Department of Engineering, University of Palermo, 90128 Palermo, Italy*

Andrea Locatelli − *Department of Information Engineering, University of Brescia, 25123 Brescia, Italy*

Luca Carletti − *Department of Information Engineering, University of Brescia, 25123 Brescia, Italy;* orcid.org/0000-0001-6268-9817

Alexey Fedorov − *Institute of Photonics and of Nanotechnologies- National Researcher Council (IFN-CNR), LNESS Laboratory, 20133 Milano, Italy*

Chiara Trovatello − *Department of Physics, Politecnico of Milano, 20133 Milano, Italy;* orcid.org/0000-0002-8150-9743

Giuseppe Di Blasio − *Department of Physics, Politecnico of Milano, 20133 Milano, Italy*

Ilaria Bargigia − *Department of Physics, Politecnico of Milano, 20133 Milano, Italy*

Charalambos Louca − *Department of Physics, Politecnico of Milano, 20133 Milano, Italy; Department of Physics, Cavendish Laboratory, Cambridge CB3 0HE, U.K.;* orcid.org/0000-0002-1122-3133

Paolo Gubian − *Department of Information Engineering, University of Brescia, 25123 Brescia, Italy*

Giulio Tavani − *Department of Physics, Politecnico of Milano, 20133 Milano, Italy*

Luca Lovisolo − *Matériaux et Phénomènes Quantiques, Université Paris Cité and CNRS, 75013 Paris, France*

Artur Tuktamyshev − *Department of Material Science, University of Milano Bicocca, 20126 Milano, Italy*

Lucio C. Andreani − *Department of Physics, University of Pavia, I-27100 Pavia, Italy;* orcid.org/0000-0003-4926-1749

Matteo Galli − *Department of Physics, University of Pavia, I-27100 Pavia, Italy*

Giulio Cerullo − *Department of Physics, Politecnico of Milano, 20133 Milano, Italy;* orcid.org/0000-0002-9534-2702

Giuseppe Leo − *Matériaux et Phénomènes Quantiques, Université Paris Cité and CNRS, 75013 Paris, France;* orcid.org/0000-0001-6525-6734

Stefano Sanguinetti − *Department of Material Science, University of Milano Bicocca, 20126 Milano, Italy;* orcid.org/0000-0002-4025-2080

Costantino De Angelis − *Department of Information Engineering, University of Brescia, 25123 Brescia, Italy;* orcid.org/0000-0001-8029-179X

Monica Bollani − *Institute of Photonics and of Nanotechnologies- National Researcher Council (IFN-CNR), LNESS Laboratory, 20133 Milano, Italy*

Complete contact information is available at: https://pubs.acs.org/10.1021/acsnano.4c13327

Notes

The authors declare no competing financial interest.

ACKNOWLEDGMENTS

The authors acknowledge financial support by the European Union—Next Generation EU, Mission 4 Component 1—

PRIN 2022 project GRACE6G(2022H7RR4F), PRIN 2022 PNRR project FLAIRS (P2022RFF9K), and PNRR MUR project PE0000023—NQSTI and project CN00000013 ICSC. A.T. acknowledges the financial support from the European Union through "FESR o FSE, PON Ricerca e Innovazione 2014-2020—DM 1062/2021" and the University of Palermo through "Fondo Finalizzato alla Ricerca di Ateneo 2024 (FFR2024)". The authors acknowledge the HORIZON EUROPE European Innovation Council (101130384, HORIZONEIC-2023-PATHFINDEROPEN-01, QUONDENSATE). C.T. acknowledges the European Union's Horizon Europe research and innovation programme under the Marie Skłodowska-Curie PIONEER HORIZON-MSCA-2021-PF-GF grant agreement No. 101066108. C.T. and G.C. acknowledge funding from the European Union—NextGenerationEU under the National Quantum Science and Technology Institute (NQSTI) Grant No. PE00000023-q-ANTHEM-CUP H43C22000870001.

REFERENCES

(1) Yang, L.; Zhang, S.; Xu, B.; Jiang, J.; Cai, B.; Lv, X.; Zou, Y.; Fan, Z.; Yang, H.; Zeng, H. I−III−VI Quantum Dots and Derivatives: Design, Synthesis, and Properties for Light-Emitting Diodes. *Nano Lett.* **2023**, *23*, 2443−2453.

(2) Vaskin, A.; Liu, S.; Addamane, S.; Vabishchevich, P. P.; Yang, Y.; Balarishnan, G.; Sinclair, M. B.; Pertsch, T.; Brener, I.; Staude, I. Manipulation of quantum dot emission with semiconductor metasurfaces exhibiting magnetic quadrupole resonances. *Opt. Express* **2021**, *29*, 5567−5579.

(3) Ropp, C.; Cummins, Z.; Nah, S.; Fourkas, J. T.; Shapiro, B.; Waks, E. Nanoscale imaging and spontaneous emission control with a single nano-positioned quantum dot. *Nat. Commun.* **2013**, *4*, 1447.

(4) Lodahl, P.; Mahmoodian, S.; Stobbe, S. Interfacing single photons and single quantum dots with photonic nanostructures. *Rev. Mod. Phys.* **2015**, *87*, 347−400.

(5) Arakawa, Y.; Holmes, M. J. Progress in quantum-dot single photon sources for quantum information technologies: A broad spectrum overview. *Appl. Phys. Rev.* **2020**, *7*, No. 021309.

(6) Tomm, N.; Javadi, A.; Antoniadis, N. O.; Najer, D.; Löbl, M. C.; Korsch, A. R.; Schott, R.; Valentin, S. R.; Wieck, A. D.; Ludwig, A.; et al. A bright and fast source of coherent single photons. *Nat. Nanotechnol.* **2021**, *16*, 399−403.

(7) Somaschi, N.; Giesz, V.; De Santis, L.; Loredo, J.; Almeida, M. P.; Hornecker, G.; Portalupi, S. L.; Grange, T.; Anton, C.; Demory, J.; et al. Near-optimal single-photon sources in the solid state. *Nat. Photonics* **2016**, *10*, 340−345.

(8) Wang, H.; Duan, Z.-C.; Li, Y.-H.; Chen, S.; Li, J.-P.; He, Y.-M.; Chen, M.-C.; He, Y.; Ding, X.; Peng, C.-Z.; et al. Near-transform-limited single photons from an efficient solid-state quantum emitter. *Phys. Rev. Lett.* **2016**, *116*, No. 213601.

(9) Wang, H.; He, Y.-M.; Chung, T.-H.; Hu, H.; Yu, Y.; Chen, S.; Ding, X.; Chen, M.-C.; Qin, J.; Yang, X.; et al. Towards optimal single-photon sources from polarized microcavities. *Nat. Photonics* **2019**, *13*, 770−775.

(10) Uppu, R.; Pedersen, F. T.; Wang, Y.; Olesen, C. T.; Papon, C.; Zhou, X.; Midolo, L.; Scholz, S.; Wieck, A. D.; Ludwig, A.; et al. Scalable integrated single-photon source. *Sci. Adv.* **2020**, *6*, No. eabc8268.

(11) Arcari, M.; Söllner, I.; Javadi, A.; Lindskov Hansen, S.; Mahmoodian, S.; Liu, J.; Thyrrestrup, H.; Lee, E. H.; Song, J. D.; Stobbe, S.; et al. Near-unity coupling efficiency of a quantum emitter to a photonic crystal waveguide. *Physical review letters* **2014**, *113*, No. 093603.

(12) Liu, F.; Brash, A. J.; O'Hara, J.; Martins, L. M.; Phillips, C. L.; Coles, R. J.; Royall, B.; Clarke, E.; Bentham, C.; Prtljaga, N.; et al. High Purcell factor generation of indistinguishable on-chip single photons. *Nature Nanotechnol.* **2018**, *13*, 835−840.

(13) Da Lio, B.; Faurby, C.; Zhou, X.; Chan, M. L.; Uppu, R.; Thyrrestrup, H.; Scholz, S.; Wieck, A. D.; Ludwig, A.; Lodahl, P.; Midolo, L.; et al. A pure and indistinguishable single-photon source at telecommunication wavelength. *Adv. Quantum Technol.* **2022**, *5*, No. 2200006.

(14) Lee, J. Y.; Miroshnichenko, A. E.; Lee, R.-K. Simultaneously nearly zero forward and nearly zero backward scattering objects. *Opt. Express* **2018**, *26*, 30393.

(15) Liu, W.; Kivshar, Y. S. Generalized Kerker effects in nanophotonics and meta-optics [Invited]. *Opt. Express* **2018**, *26*, 13085.

(16) Bukharin, M. M.; Pecherkin, V. Y.; Ospanova, A. K.; Il'in, V. B.; Vasilyak, L. M.; Basharin, A. A.; Luk'yanchuk, B. Transverse Kerker effect in all-dielectric spheroidal particles. *Sci. Rep.* **2022**, *12*, 7997.

(17) Khokhar, M.; Inam, F. A.; Nair, R. V. Kerker Condition for Enhancing Emission Rate and Directivity of Single Emitter Coupled to Dielectric Metasurfaces. *Adv. Opt. Mater.* **2022**, *10*, No. 2200978.

(18) Person, S.; Jain, M.; Lapin, Z.; Sáenz, J. J.; Wicks, G.; Novotny, L. Demonstration of zero optical backscattering from single nanoparticles. *Nano Lett.* **2013**, *13*, 1806−1809.

(19) Li, R.; Zhou, X.; Panmai, M.; Xiang, J.; Liu, H.; Ouyang, M.; Fan, H.; Dai, Q.; Wei, Z. Broadband zero backward scattering by all-dielectric core-shell nanoparticles. *Opt. Express* **2018**, *26*, 28891−28901.

(20) Fu, Y. H.; Kuznetsov, A. I.; Miroshnichenko, A. E.; Yu, Y. F.; Luk'yanchuk, B. Directional visible light scattering by silicon nanoparticles. *Nat. Commun.* **2013**, *4*, 1527.

(21) Rocco, D.; Carletti, L.; Locatelli, A.; De Angelis, C. Controlling the directivity of all-dielectric nanoantennas excited by integrated quantum emitters. *J. Opt. Soc. Am. B* **2017**, *34*, 1918.

(22) Di Francescantonio, A.; Zilli, A.; Rocco, D.; Coudrat, L.; Conti, F.; Biagioni, P.; Duò, L.; Lemaître, A.; De Angelis, C.; Leo, G.; et al. All-optical free-space routing of upconverted light by metasurfaces via nonlinear interferometry. *Nat. Nanotechnol.* **2024**, *19*, 298−305.

(23) Fagiani, L.; Bolzonello, L.; Osmond, J.; de Ceglia, D.; van Hulst, N.; Bollani, M.; Vincenti, M. A. Dual-Mode Polarization Control with Quasi-Bound States in the Continuum. *Adv. Opt. Mater.* **2018**, *12*, No. 2301456.

(24) Khorasaninejad, M.; Capasso, F. Metalenses: Versatile multifunctional photonic components. *Science* **2017**, *358*, No. eaam8100.

(25) Zotev, P. G.; Wang, Y.; Sortino, L.; Severs Millard, T.; Mullin, N.; Conteduca, D.; Shagar, M.; Genco, A.; Hobbs, J. K.; Krauss, T. F.; et al. Transition Metal Dichalcogenide Dimer Nanoantennas for Tailored Light−Matter Interactions. *ACS Nano* **2022**, *16*, 6493−6505.

(26) Sortino, L.; Zotev, P.; Mignuzzi, S.; Cambiasso, J.; Schmidt, D.; Genco, A.; Aßmann, M.; Bayer, M.; Maier, S.; Sapienza, R.; et al. Enhanced light-matter interaction in an atomically thin semiconductor coupled with dielectric nano-antennas. *Nat. Commun.* **2019**, *10*, 5119.

(27) Fagiani, L.; Gandolfi, M.; Carletti, L.; de Angelis, C.; Osmond, J.; Bollani, M. Modelling and nanofabrication of chiral dielectric metasurfaces. *Micro and Nano Engineering* **2023**, *19*, No. 100187.

(28) Solntsev, A. S.; Agarwal, G. S.; Kivshar, Y. S. Metasurfaces for quantum photonics. *Nat. Photonics* **2021**, *15*, 327−336.

(29) Rutckaia, V.; Heyroth, F.; Novikov, A.; Shaleev, M.; Petrov, M.; Schilling, J. Quantum dot emission driven by Mie resonances in silicon nanostructures. *Nano Lett.* **2017**, *17*, 6886−6892.

(30) Bouchet, D.; Mivelle, M.; Proust, J.; Gallas, B.; Ozerov, I.; Garcia-Parajo, M. F.; Gulinatti, A.; Rech, I.; De Wilde, Y.; Bonod, N.; et al. Enhancement and inhibition of spontaneous photon emission by resonant silicon nanoantennas. *Physical Review Applied* **2016**, *6*, No. 064016.

(31) Staude, I.; Khardikov, V. V.; Fofang, N. T.; Liu, S.; Decker, M.; Neshev, D. N.; Luk, T. S.; Brener, I.; Kivshar, Y. S. Shaping photoluminescence spectra with magnetoelectric resonances in all-dielectric nanoparticles. *Acs Photonics* **2015**, *2*, 172−177.

https://doi.org/10.1021/acsnano.4c13327
ACS Nano 2025, 19, 3500−3509

(32) Sortino, L.; Zotev, P. G.; Phillips, C. L.; Brash, A. J.; Cambiasso, J.; Marensi, E.; Fox, A. M.; Maier, S. A.; Sapienza, R.; Tartakovskii, A. I. Bright single photon emitters with enhanced quantum efficiency in a two-dimensional semiconductor coupled with dielectric nano-antennas. *Nat. Commun.* **2021**, *12*, 6063.
(33) Kroychuk, M. K.; Shorokhov, A. S.; Yagudin, D. F.; Rakhlin, M. V.; Klimko, G. V.; Toropov, A. A.; Shubina, T. V.; Fedyanin, A. A. Quantum Dot Photoluminescence Enhancement in GaAs Nanopillar Oligomers Driven by Collective Magnetic Modes. *Nanomaterials* **2023**, *13*, 507.
(34) Veeken, T.; Daiber, B.; Agrawal, H.; Aarts, M.; Alarcón-Lladó, E.; Garnett, E. C.; Ehrler, B.; van de Groep, J.; Polman, A. Directional quantum dot emission by soft-stamping on silicon Mie resonators. *Nanoscale Advances* **2022**, *4*, 1088−1097.
(35) Rocco, D.; Locatelli, A.; Carletti, L.; Vincenti, M. A.; De Angelis, C. Nonlinear asymmetric imaging with AlGaAs metasurface. *Opt. Express* **2024**, *32*, 11673−11680.
(36) Siampour, H.; Wang, O.; Zenin, V. A.; Boroviks, S.; Siyushev, P.; Yang, Y.; Davydov, V. A.; Kulikova, L. F.; Agafonov, V. N.; Kubanek, A.; et al. Ultrabright single-photon emission from germanium-vacancy zero-phonon lines: deterministic emitter-waveguide interfacing at plasmonic hot spots. *Nanophotonics* **2020**, *9*, 953−962.
(37) Siampour, H.; O'Rourke, C.; Brash, A. J.; Makhonin, M. N.; Dost, R.; Hallett, D. J.; Clarke, E.; Patil, P. K.; Skolnick, M. S.; Fox, A. M. Observation of large spontaneous emission rate enhancement of quantum dots in a broken-symmetry slow-light waveguide. *npj Quantum Inf.* **2023**, *9*, 15.
(38) Gurioli, M.; Wang, Z.; Rastelli, A.; Kuroda, T.; Sanguinetti, S. Droplet epitaxy of semiconductor nanostructures for quantum photonic devices. *Nat. Mater.* **2019**, *18*, 799.
(39) Watanabe, K.; Koguchi, N.; Gotoh, Y. Fabrication of GaAs Quantum Dots by Modified Droplet Epitaxy. *Jpn. J. Appl. Phys.* **2000**, *39*, L79.
(40) Tuktamyshev, A.; Fedorov, A.; Bietti, S.; Vichi, S.; Zeuner, K. D.; Jöns, K. D.; Chrastina, D.; Tsukamoto, S.; Zwiller, V.; Gurioli, M.; Sanguinetti, S. Telecom-wavelength InAs QDs with low fine structure splitting grown by droplet epitaxy on GaAs(111)A vicinal substrates. *Appl. Phys. Lett.* **2021**, *118*, No. 133102.
(41) Basso Basset, F.; Bietti, S.; Tuktamyshev, A.; Vichi, S.; Bonera, E.; Sanguinetti, S. Spectral broadening in self-assembled GaAs quantum dots with narrow size distribution. *J. Appl. Phys.* **2019**, *126*, No. 024301.
(42) Bietti, S.; Basset, F. B.; Tuktamyshev, A.; Bonera, E.; Fedorov, A.; Sanguinetti, S. High−temperature droplet epitaxy of symmetric GaAs/AlGaAs quantum dots. *Sci. Rep.* **2020**, *10*, 6532.
(43) Sanguinetti, S.; Bietti, S.; Koguchi, N. *Droplet epitaxy of nanostructures*; Elsevier, 2018; 293−314.
(44) Ohtake, A. Surface reconstructions on GaAs(001). *Surf. Sci. Rep.* **2008**, *63*, 295−327.
(45) Horikoshi, Y.; Kawashima, M.; Yamaguchi, H. Migration-Enhanced Epitaxy of GaAs and AlGaAs. *Jpn. J. Appl. Phys.* **1988**, *27*, 169.
(46) Tognazzi, A.; Okhlopkov, K. I.; Zilli, A.; Rocco, D.; Fagiani, L.; Mafakheri, E.; Bollani, M.; Finazzi, M.; Celebrano, M.; Shcherbakov, M. R.; et al. Third-harmonic light polarization control in magnetically resonant silicon metasurfaces. *Opt. Express* **2021**, *29*, 11605−11612.
(47) Tavani, G.; Chiappini, A.; Fedorov, A.; Scotognella, F.; Sanguinetti, S.; Chrastina, D.; Bollani, M. Tailoring of embedded dielectric alumina film in AlGaAs epilayer by selective thermal oxidation. *Optical Materials Express* **2022**, *12*, 835.
(48) Carletti, L.; Rocco, D.; Locatelli, A.; De Angelis, C.; Gili, V. F.; Ravaro, M.; Favero, I.; Leo, G.; Finazzi, M.; Ghirardini, L.; Celebrano, M.; Marino, G.; Zayats, A. V. Controlling second-harmonic generation at the nanoscale with monolithic AlGaAs-on-AlOx antennas. *Nanotechnology* **2017**, *28*, No. 114005.
(49) Jahan, K. L.; Boda, A.; Shankar, I.; Raju, C. N.; Chatterjee, A. Magnetic field effect on the energy levels of an exciton in a GaAs quantum dot: Application for excitonic lasers. *Sci. Rep.* **2018**, *8*, 5073.
(50) Genco, A.; Cruciano, C.; Corti, M.; McGhee, K. E.; Ardini, B.; Sortino, L.; Huttenhofer, L.; Virgili, T.; Lidzey, D. G.; Maier, S. A.; et al. k-Space hyperspectral imaging by a birefringent common-path interferometer. *ACS photonics* **2022**, *9*, 3563−3572.

https://doi.org/10.1021/acsnano.4c13327
ACS Nano 2025, 19, 3500−3509